Environmental Science & Technology
Article
pubs.acs.org/est

Environment-Friendly Carbon Quantum Dots/$ZnFe_2O_4$ Photocatalysts: Characterization, Biocompatibility, and Mechanisms for NO Removal

Yu Huang,*[†,‡] Yanling Liang,[†] Yongfang Rao,[§] Dandan Zhu,[†] Jun-ji Cao,[†,‡] Zhenxing Shen,[§] Wingkei Ho,[∥] and Shun Cheng Lee[⊥]

[†]Key Laboratory of Aerosol Chemistry and Physics, Institute of Earth Environment, Chinese Academy of Sciences, Xi'an 710061, China

[‡]State Key Lab of Loess and Quaternary Geology (SKLLQG), Institute of Earth Environment, Chinese Academy of Sciences, Xi'an 710061, China

[§]Department of Environmental Science and Engineering, Xi'an Jiaotong University, Xi'an 710049, China

[∥]Department of Science and Environmental Studies, The Education University of Hong Kong, Hong Kong, China

[⊥]Department of Civil and Environmental Engineering, The Hong Kong Polytechnic University, Hung Hom, Hong Kong, China

Supporting Information

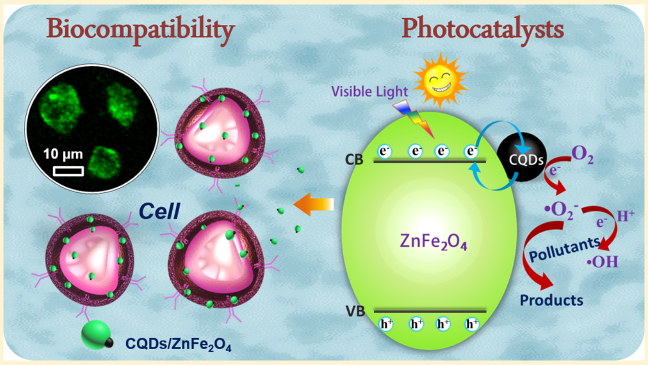

ABSTRACT: A highly efficient and environmentally-friendly oxidation process is always desirable for air purification. This study reported a novel carbon quantum dots (CQDs)/$ZnFe_2O_4$ composite photocatalyst for the first time through a facile hydrothermal process. The CQDs/$ZnFe_2O_4$ (15 vol %) composite demonstrates stronger transient photocurrent response, approximately 8 times higher than that of $ZnFe_2O_4$, indicating superior transfer efficiency of photogenerated electrons and separation efficiency of photogenerated electron−hole pairs. Compared with pristine $ZnFe_2O_4$ nanoparticles, CQDs/$ZnFe_2O_4$ displayed enhanced photocatalytic activities on gaseous NO_x removal and high selectivity for nitrate formation under visible light ($\lambda > 420$ nm) irradiation. Electron spin resonance analysis and a series of radical-trapping experiments showed that the reactive species contributing to NO elimination were $\cdot O_2^-$ and $\cdot OH$ radicals. The possible mechanisms were proposed regarding how CQDs improve the photocatalytic performance of $ZnFe_2O_4$. The CQDs are believed to act as an electron reservoir and transporter as well as a powerful energy-transfer component during the photocatalysis processes over CQDs/$ZnFe_2O_4$ samples. Furthermore, the toxicity assessment authenticated good biocompatibility and low cytotoxicity of CQDs/$ZnFe_2O_4$. The results of this study indicate that CQDs/$ZnFe_2O_4$ is a promising photocatalyst for air purification.

■ INTRODUCTION

Nitrogen oxides (NO_x), one of secondary aerosol precursors, generally derive from the combustion of fossil fuels.[1] It was unveiled that secondary aerosol formation correlated closely with haze events in China.[2] NO_x was also found to make a significant contribution to other environmental problems such as photochemical smog and acid rain. Over the past decades, the rapid growth of energy consumption resulted in the substantial increase of NO_x concentration in atmosphere,[3] receiving extensive concern. With the aim of removing NO_x from combustion off-gas, varied technologies such as three-way catalysis and selective catalytic reduction have been developed and proven effective.[4−6] However, these deNO_x technologies are not economically feasible to eliminate NO_x at parts per billion (ppb) level in the ambient air.

Photocatalytic oxidation is a green and simple alternative for NO_x degradation at ppb levels.[7−9] For instance, Fe_2O_3-based materials have been utilized as photocatalysts to remove NO_x by Balbuena et al.[10,11] NO_x can be oxidized to nitrate by photocatalysis, whereas some NO is also converted into undesirable NO_2. Therefore, high conversion and selectivity for nitrate formation are equally crucial. Spinel-type oxides, with a general formula of AB_2O_4, are promising heterogeneous catalysts due to their flexible chemical composition and structural stability.[12−14] The photostability and visible light absorption ability of spinels have spawned ever growing

Received: September 1, 2016
Revised: December 29, 2016
Accepted: February 1, 2017
Published: February 1, 2017

DOI: 10.1021/acs.est.6b04460
Environ. Sci. Technol. 2017, 51, 2924−2933

interests in the field of photocatalysis.[15,16] As a p-type semiconductor, zinc ferrite ($ZnFe_2O_4$), with a relatively narrow band gap of 1.96 eV and a strong visible light response, has attracted lots of attention in H_2 generation[17,18] and organic pollutant removal.[19−21] However, the rapid recombination of photogenerated electron−hole pairs repressed the photocatalytic activity of $ZnFe_2O_4$.[22] It is a better choice to use $ZnFe_2O_4$ as a sensitizer for wide-bandgap semiconductors[23,24] or combine $ZnFe_2O_4$ with other functional materials which can increase separation efficiency of photogenerated electron−hole pairs.[25,26] Although these strategies could help the separation of photoinduced carriers to some degree, these composite catalysts are still far from enough for potential applications. Thus, it is imperative to further improve the photocatalytic activity and the utilization of solar light to meet the requirements of potential industrial applications.

In recent years, carbon quantum dots (CQDs), a novel carbon nanomaterial with sizes below 10 nm, have found wide applications such as fluorescent probes,[27] photovoltaic devices,[28] bioimaging[29] and so on, thanks to its excellent optical properties, chemical stability, intrinsic low toxicity, and eco-friendliness.[30] The conjugated π structure of CQDs makes them excellent electron transporters and acceptors.[31] Furthermore, CQDs have been shown to possess upconversion photoluminescence (PL) properties.[32−34] These characteristics endow CQDs with the potential to modify the semiconductors to improve their photocatalytic activities and the utilization of solar light, such as SiO_2,[33] TiO_2,[35−37] Fe_2O_3,[38,39] Ag_3PO_4,[40] Cu_2O,[41,42] ZnO,[43] CdS,[44] g-C_3N_4,[45] $BiVO_4$,[46] Bi_2WO_6,[31] Bi_2MoO_6,[47] BiOCl,[48] and BiOI.[49] However, the information is limited, regarding the modifiability of spinel $ZnFe_2O_4$ by CQDs.

The continuing increase in applications of nanomaterials has incurred considerable environmental, health, and safety concerns in recent years. Silica nanoparticles were reported to affect the expression of some genes in zebrafish embryos;[50] CuO was observed to inhibit seedling growth of different *Arabidopsis thaliana* ecotypes as well as the germination of their pollens and seeds;[51] Kim et al. reported Al_2O_3, CeO_2, TiO_2, and ZnO exhibited cytotoxicity to human lung cells with different degree.[52] When human keratinocytes were exposed for 24 and 48 h to Ag nanoparticles, cell proliferation, and viability decreased.[53] Thus, the potential harmful effects of nanoparticles should be properly evaluated on humans prior to their use.

In this study, we report a facile hydrothermal method to prepare CQDs/$ZnFe_2O_4$ nanoparticles (NPs), which exhibited enhanced photocatalytic performance to remove ppb-level NO under visible light. The CQDs/$ZnFe_2O_4$ NPs also showed a high selectivity for nitrate formation. The phase, morphologies, microstructures, and optical properties of the prepared catalysts were investigated in detail. The key role of CQDs in the enhancement of photocatalytic activity was elucidated, and the possible photocatalytic mechanism was proposed. The cytotoxicity of CQDs/$ZnFe_2O_4$ nanoparticles was also evaluated toward human lung cells.

■ EXPERIMENTAL SECTION

Preparation of CQDs, $ZnFe_2O_4$, and CQDs/$ZnFe_2O_4$ NPs. CQDs were synthesized using a one-step hydrothermal process as described by Wu.[54] L-ascorbic acid (1.6 g), glycol (15 mL), and deionized water (25 mL) were mixed in a beaker. The mixture was stirred vigorously for 30 min to obtain homogeneity, placed in a 50 mL Teflon-lined stainless autoclave, and then heated at 160 °C for 70 min. The product was naturally cooled to room temperature, and a light yellow solution was obtained. The product was collected and filtered with an ultrafiltration membrane (0.2 μm) to remove impurities and large particles. Finally, a yellow aqueous solution containing CQDs was obtained.

In a typical synthesis procedure, 4 mmol of $Zn(NO_3)_2\cdot6H_2O$ and 8 mmol of $Fe(NO_3)_3\cdot9H_2O$ were dissolved in 20 mL of deionized water under vigorous stirring until a homogeneous aqueous solution was obtained. The solution pH was adjusted to 13 using sodium hydroxide solution (2 M). The resulting dark brown slurry and CQDs aqueous solution were transferred into a 100 mL Teflon-lined stainless-steel autoclave and maintained at 100 °C for 6 h. Then, the autoclave was naturally cooled to ambient temperature. Finally, the samples were washed several times with deionized water and ethanol before drying at 70 °C overnight. Pure $ZnFe_2O_4$ and CQDs/$ZnFe_2O_4$ with different volume ratios (5%, 15%, and 25%) were synthesized using a similar route by tuning the dosage of the CQDs aqueous solution.

Photocatalyst Characterization. Powder X-ray diffraction (XRD) was performed with a Philips X'pert PRO SUPER diffractometer using Cu Kα (λ = 0.154 06 nm) radiation at 40 kV and 40 mA with a scanning rate of 0.04° 2θ s^{-1} in the 2θ range of 10°−80°. Chemical composition was analyzed using X-ray photoelectron spectroscopy (XPS; VG, Physical Electrons Quantum2000 Scanning Esca Microprob, Al Ka radiation). The binding energies were normalized to the signal for adventitious carbon at 284.8 eV. The morphology and structure of the samples were characterized via transmission electron microscopy (TEM, JEM-2010, Japan). The Brunauer−Emmett−Teller (BET) surface area and pore structure of $ZnFe_2O_4$ were obtained from N_2 adsorption/desorption isotherms at 77 K using an ASAP 2020 automatic analyzer (Micromeritics Instrument Corp., Norcross, GA, U.S.A.). A Varian Cary 100 Scan UV−visible system equipped with a labsphere diffuse reflectance accessory was used to obtain the reflectance spectra of the catalysts over the range of 200−800 nm. Labsphere USRS-99-010 was employed as a reflectance standard. The spectra were converted from reflection to absorbance using the Kubelka−Munk method. Samples for electron spin resonance spectroscopy (ESR, ER200-SRC, Bruker, Germany) were prepared by dispersing 0.05 g of photocatalyst into 25 mM 5, 5′-dimethyl-1-pirroline-*N*-oxide (DMPO) solution for DMPO−·OH or 50 mL methanol dispersion for DMPO−·O_2^-, respectively. The light irradiation source was a 300 W Xe arc lamp (PLS-SXE 300, Beijing). The visible light used in this study was obtained by cutting UV light (λ < 420 nm) with a filter.

Photoelectrochemical Measurements. The photoelectrochemical properties of $ZnFe_2O_4$ and CQDs/$ZnFe_2O_4$ (15 vol %) were evaluated using a Parstat4000 electrochemical workstation (Princeton, USA) in a conventional three-electrode cell. A platinum plate and an Ag/AgCl electrode were used as the counter and reference electrodes, respectively. The working electrode was fabricated by dispersing 25 mg of sample into 5 mL of 1 wt % Nafion ethanol solution to obtain a homogeneous suspension through bath sonication. The films were modified on a fluorine-doped tin oxide-conducting glass by dip coating and then dried at room temperature. The current−time curves were measured at 0.5 V vs Ag/AgCl in 0.1 mol L^{-1} Na_2SO_4 at ambient temperature under a 100 W LED lamp (λ = 420 nm).

DOI: 10.1021/acs.est.6b04460
Environ. Sci. Technol. 2017, 51, 2924−2933

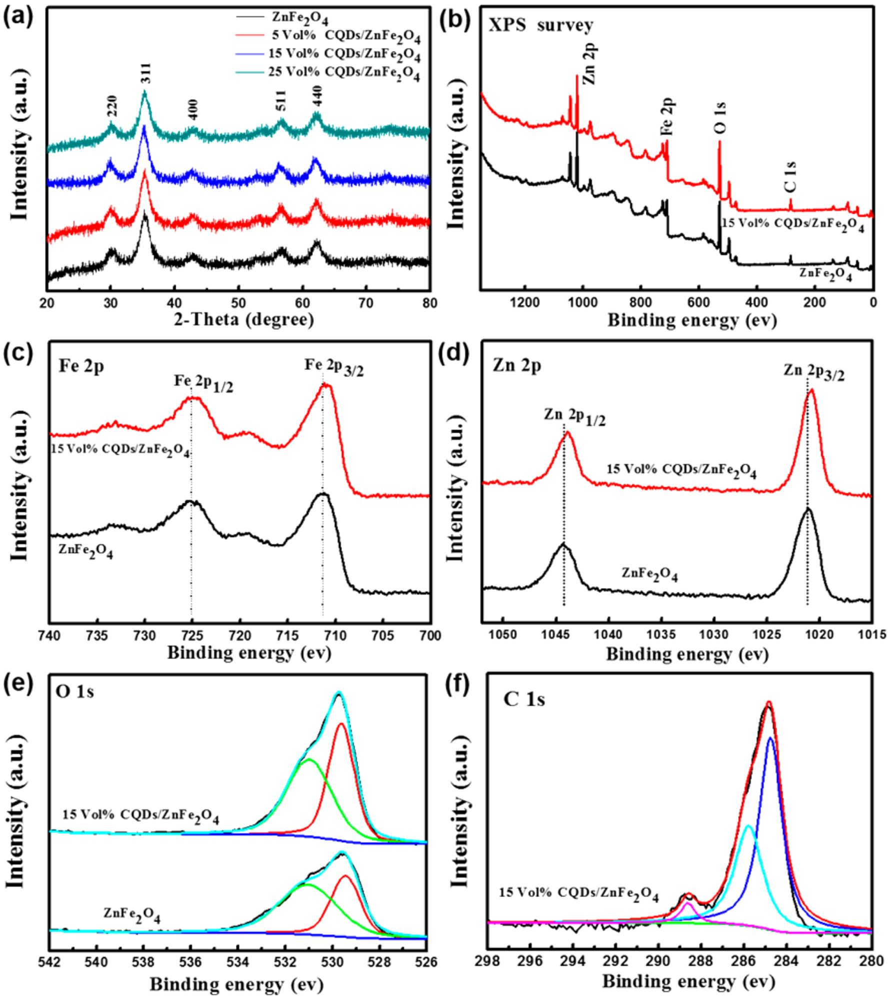

Figure 1. (a) XRD patterns of $ZnFe_2O_4$ and CQDs/$ZnFe_2O_4$ with different CQDs loading amount. (b) XPS survey spectra of $ZnFe_2O_4$ and CQDs/$ZnFe_2O_4$ (15 vol %). High resolution XPS spectra of (c) Fe 2p, (d) Zn 2p, (e) O 1s, and (f) C 1s in corresponding samples.

Evaluation of Photocatalytic Activity. The photocatalytic activities of $ZnFe_2O_4$ and CQDs/$ZnFe_2O_4$ were investigated on NO degradation. The reaction chamber was composed of a rectangular stainless steel vessel (30 × 15 × 10 cm^3) and covered with a quartz window. Visible light was supplied by a 300 W xenon lamp (Perfect Light MICROSOLAR 300, Beijing, China) vertically passed through the quartz window. A piece of UV cutoff glass was employed for the visible-light-driven photocatalysis to remove UV light with wavelengths below 420 nm. One sample dish (with a diameter of 9 cm) containing the photocatalyst powders (0.1 g) was placed at the center of the reactor for each photocatalytic activity test. The distance between the light source and the catalyst was maintained at 20 cm. The intensity of light resource was controlled at 0.96 W/cm^2 by using a photometer (THORLABS PD130, U.S.A.). The photocatalyst samples were prepared by coating an aqueous suspension of $ZnFe_2O_4$ and CQDs/$ZnFe_2O_4$ products onto a glass dish. The photocatalyst (0.1 g) was dispersed in 20 mL of distilled water in a beaker by ultrasonic treatment for 15 min and then coated onto glass dishes with a diameter of 9 cm. The dishes containing the photocatalyst were pretreated at 70 °C for several hours until water was completely removed from the suspension. Then, the dishes were cooled to room temperature before the photocatalytic test.

NO gas was acquired from a compressed gas cylinder with an initial concentration of 50 ppm. The initial NO concentration for photocatalytic test was diluted to 400 ppb by the air stream supplied by a zero-air generator (Model 1001, Sabio Instruments LLC, Georgetown, TX, U.S.A.). The gas streams were premixed completely by a gas blender, and the flow rate was controlled at 3 L min^{-1} by a mass flow controller. The Xe lamp was switched on after the catalyst achieved adsorption/desorption equilibrium. NO and NO_2 concentrations were continuously measured by a chemiluminescence NO_x analyzer (Model 42c, Thermo Environmental Instruments Inc., Franklin, MA, U.S.A.) during photocatalytic degradation, with a sampling rate of 0.7 L min^{-1}. The reaction of NO with air was negligible when a control experiment was performed with or without light in the absence of the photocatalyst.

To evaluate the photocatalytic performance of the as-prepared samples for NO_x elimination from the environment, the photocatalytic activity tests under UV−vis light irradiation with the same samples and P25 were also conducted under identical conditions with visible-light activity measurements except for the nonuse of optical filter.

The intermediates and final products (nitrate and nitrite ions) remaining in the catalyst powders after the photocatalytic activity test were extracted by immersing the powders in deionized water (10 mL) and then subjected to ion

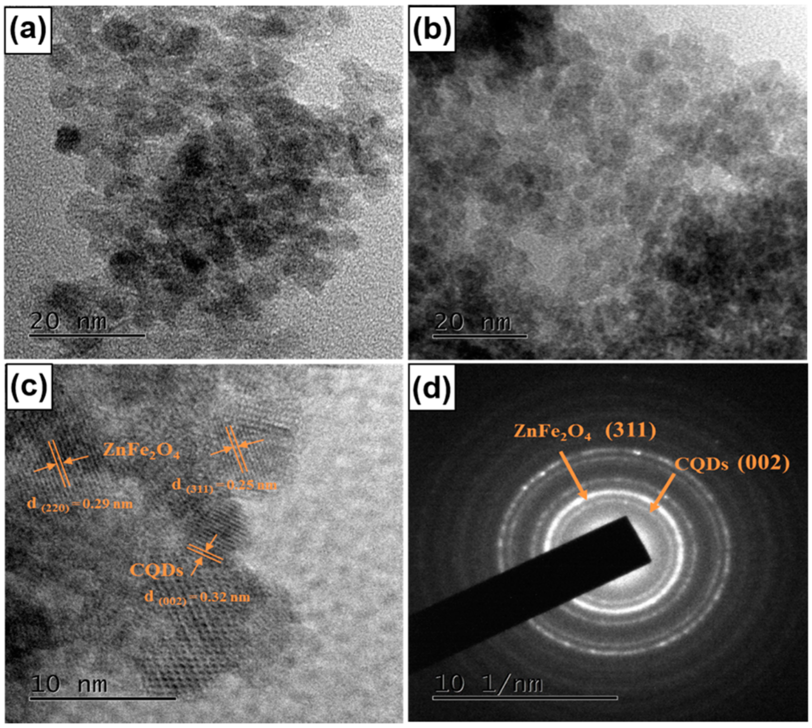

Figure 2. TEM images of $ZnFe_2O_4$ and CQDs/$ZnFe_2O_4$ (15 vol %) (a,b); high resolution TEM and SAED images of CQDs/$ZnFe_2O_4$ (15 vol %) (c,d).

chromatography using a Dionex-600 Ion Chromatograph (Dionex Inc., Sunnyvale, CA, U.S.A.) equipped with an IonPac AS14A column. The mobile phase was composed of a mixture of 1.8 mM Na_2CO_3 and 1.7 mM $NaHCO_3$ at a flow rate of 1.20 mL min^{-1}, and the injected sample volume was 20 μL. The detection limits for NO_2^- and NO_3^- were 5 and 25.6 μg L^{-1}, respectively.

Cytotoxicity Assay. Human alveolar epithelial (A549) cell line was used to investigate cell growth inhibition of $ZnFe_2O_4$ and CQDs/$ZnFe_2O_4$ nanoparticles. A549 cells were cultured with Dulbecco's Modified Eagle's Medium (DMEM, GIBCO) supplemented with 10% fetal bovine serum (FBS, GIBCO), 1% penicillin (Sigma), and streptomycin (Sigma) at 37 °C in 5% CO_2.

The cytotoxicity test of $ZnFe_2O_4$ and CQDs/$ZnFe_2O_4$ to A549 cells was evaluated by a modified methyl thiazolyl tetrazolium (MTT) assay.[55,56] Briefly, A549 cells (104 cells per well) were seeded in 96-well plates and allowed to adhere for 24 h under a high humidity environment with 5% CO_2 at 37 °C. The cells were then exposed to incremental concentrations, 0, 0.5, 5, 10, 25, 50, and 100 μg mL^{-1} of $ZnFe_2O_4$ and CQDs/$ZnFe_2O_4$ saline solution for 24 h, respectively. After the exposure completed, old medium was removed and cells were washed with phosphate buffered saline. Then 100 μL of serum-free DMEM containing MTT (0.5 mg·mL^{-1}) was added to each well and incubated for another 4 h at 37 °C. The culture medium was discarded, followed by the addition of 150 μL dimethyl sulfoxide (DMSO) to dissolve formazan under shaking for more than 10 min. The optical density (OD) was measured at 490 nm with a microplate reader (Multiskan GO-Thermo Scientific Inc., U.S.A.) and measurement for each treatment was repeated in triplicate. Finally, the cell viability was estimated based on the following equation:

$$\text{cell viability (\%)} = \text{OD}_{\text{treated}}/\text{OD}_{\text{control}} \times 100\%$$

where $\text{OD}_{\text{control}}$ was obtained without $ZnFe_2O_4$ and CQDs/$ZnFe_2O_4$, and $\text{OD}_{\text{treated}}$ was obtained in the presence of $ZnFe_2O_4$ and CQDs/$ZnFe_2O_4$.

Fluorescence Cellular Imaging. Cellular uptake and bioimaging of the cells were conducted via fluorescence microscopy. A549 cells were transfected with 50 μg mL^{-1} of $ZnFe_2O_4$ and CQDs/$ZnFe_2O_4$ saline solution in Φ 20 mm cell culture dishes at 37 °C. After 1 h, the cells were washed in PBS buffer. Immediately, cells were imaged using an Olympus laser-based point scanning FV 1000 confocal fluorescent microscope. A 488 nm laser was used for excitation.

■ RESULTS AND DISCUSSION

Compositional and Structural Information. The phase structures of $ZnFe_2O_4$ and CQDs/$ZnFe_2O_4$ with different CQDs loading amount were characterized via XRD. Figure 1a shows that the diffraction peaks of all samples can be attributed to $ZnFe_2O_4$ with a cubic spinel structure. The peaks at 2θ values of 29.9°, 35.2°, 42.8°, 56.6°, and 62.2° are ascribed to the (220), (311), (400), (511), and (440) reflections of $ZnFe_2O_4$ (JCPDS No. 22-1012), respectively.[57] However, no characteristic peak of CQDs (approximately 26°) can be detected in the CQDs/$ZnFe_2O_4$ materials, which may be attributed to the low content and high dispersion of the CQDs in the samples.[31] The positions of the diffraction peaks remain unchanged for CQDs/$ZnFe_2O_4$ photocatalysts, implying that the introduction of CQDs during synthesis did not affect the phase structure of $ZnFe_2O_4$.

To confirm the existence of CQDs and reveal the chemical states of synthesized materials, XPS was conducted for the CQDs/$ZnFe_2O_4$ (15 vol %) and $ZnFe_2O_4$ samples. The survey spectrum (Figure 1b) confirms that the $ZnFe_2O_4$ and CQDs/$ZnFe_2O_4$ (15 vol %) samples contain Zn, Fe, O, and C elements. The high-resolution XPS spectra of Fe 2p, Zn 2p, O

DOI: 10.1021/acs.est.6b04460
Environ. Sci. Technol. 2017, 51, 2924−2933

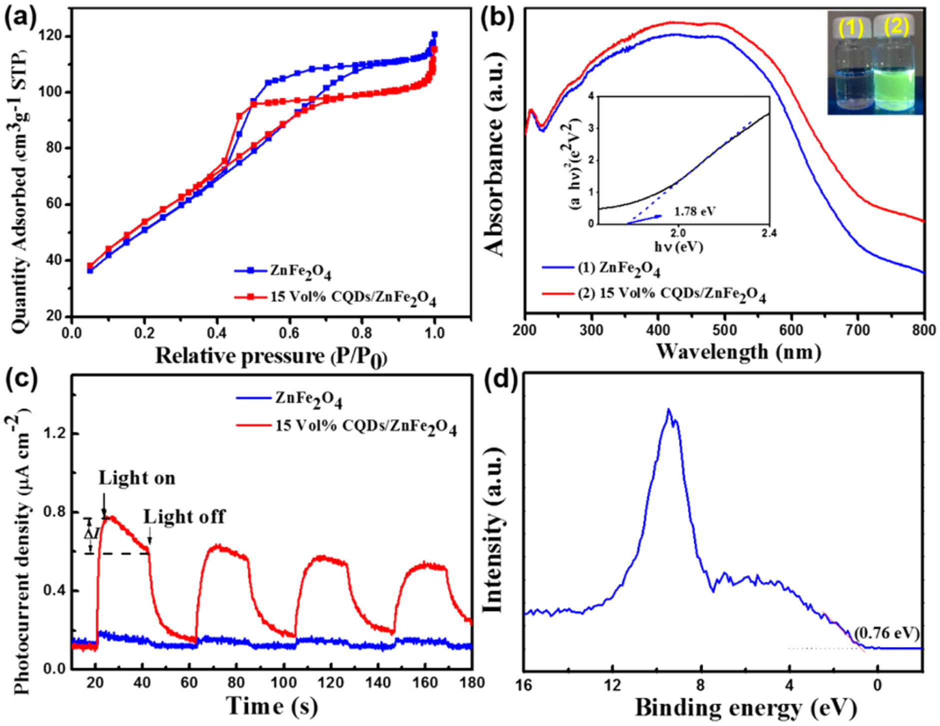

Figure 3. (a) Nitrogen adsorption−desorption isotherms of $ZnFe_2O_4$ and CQDs/$ZnFe_2O_4$ (15 vol %); (b) UV−visible diffuse reflectance spectra of $ZnFe_2O_4$and CQDs/$ZnFe_2O_4$ (15 vol %) [Inset: $(\alpha h\nu)^2$ vs $h\nu$ of pure $ZnFe_2O_4$ and the photograph of (1) water and (2) pure CQDs disperse solution with UV light (365 nm); (c) Photocurrent responses of $ZnFe_2O_4$ and CQDs/$ZnFe_2O_4$ (15 vol %) in 0.5 M Na_2SO_4 electrolyte under visible light irradiation (λ = 420 nm) and (d) valence band XPS spectra of $ZnFe_2O_4$.

1s, and C 1s are illustrated in Figures 1c−f, respectively. The two peaks at binding energies of 710.7 and 724.2 eV are characteristics of the Fe^{3+} state[58,59] (see Figure 1c). Figure 1d depicts that the two distinct peaks centered at 1022.2 and 1045.2 eV belong to the Zn $2p_{3/2}$ and Zn $2p_{1/2}$ orbitals, respectively, suggesting the oxidation state of Zn^{2+} in the sample. In comparison, the Fe 2p and Zn 2p peaks in the CQDs/$ZnFe_2O_4$ (15 vol %) sample show slight shift toward lower binding energies, which suggested that there are chemical interactions between CQDs and $ZnFe_2O_4$ materials and leads to the change of chemical environment of the surface Fe and Zn in CQDs/$ZnFe_2O_4$ (15 vol %). The O 1s core level spectrum shows a broad asymmetric curve fitted by two peaks with binding energies at 531.6 and 529.8 eV (see Figure 1e), indicating the existence of two oxygen species. The peak at 531.6 eV is the characteristic signal of oxygen in surface hydroxyl group, while the one at 529.8 eV is in good agreement with the lattice oxygen in the $ZnFe_2O_4$ crystals. Figure 1f shows the deconvoluted C 1s XPS spectrum of CQDs/$ZnFe_2O_4$ (15 vol %) . The typical peak at 284.7 eV is ascribed to the C—C bond with sp^2 orbital, and the peaks centered at 285.8 and 288.6 eV are characteristics of C—O—C and C=O bonds, respectively. Therefore, the XPS results confirms the existence of the CQDs and the interaction with $ZnFe_2O_4$.[31,47]

Morphology. The morphology and crystalline structure of the $ZnFe_2O_4$ and CQDs/$ZnFe_2O_4$ (15 vol %) materials are depicted by the TEM images in Figure 2. As shown in Figure 2a, $ZnFe_2O_4$ exists in a spherical shape with diameter approximately below 10 nm, in consistent with the broad diffraction peaks observed in the XRD pattern.[60] After modified with 4−5 nm CQDs, $ZnFe_2O_4$ largely maintains the original shape and size distribution (Figure 2b). The high-resolution TEM image (Figure 2c) of the CQDs/$ZnFe_2O_4$ (15 vol %) NPs shows lattice fringe spacing of 0.25 and 0.29 nm, which correspond well to the (111) and (220) planes of the cubic-structured $ZnFe_2O_4$, respectively. The lattice spacing of approximately 0.32 nm along the side of the $ZnFe_2O_4$ NPs corresponds to the (002) planes of graphitic carbon, demonstrating the successful coupling of the CQDs with $ZnFe_2O_4$.[61] The selected area electron diffraction (SAED) image of CQDs/$ZnFe_2O_4$ (15 vol %) shows ring patterns which is the characteristic feature of polycrystalline materials (Figure 2d). The appearance of two sets of diffraction rings further confirms the coexistence of $ZnFe_2O_4$ and CQDs.

Textural, Optical, and Electric Properties. The BET specific surface area of the pure $ZnFe_2O_4$ and CQDs/$ZnFe_2O_4$ (15 vol %) were examined by N_2 adsorption/desorption isotherms to evaluate their potential as catalytic materials, as shown in Figure 3a. The shape of the physisorption isotherm is in accordance with the type IV hysteresis loop in the P/P_0 range of 0.45−0.80, and this is the typical characteristics of mesopores structure, according to the IUPAC classification.[60] As can be seen from Table S1 of the Supporting Information, both $ZnFe_2O_4$ and CQDs/$ZnFe_2O_4$ (15 vol %) possess high BET specific surface areas, and the addition of CQDs has little effects on their surface areas and pore volume. According to the average pore diameter (as shown in Table S1), we can conclude that both $ZnFe_2O_4$ and CQDs/$ZnFe_2O_4$ display mesoporous structure, which is in consistent with the results of N_2 adsorption/desorption isotherms.

UV−visible diffuse reflectance spectra (DRS) were obtained to elucidate the optical properties of the photocatalysts, as shown in Figure 3b. $ZnFe_2O_4$ exhibits a broad absorption from UV to visible light, revealing the band gap of 1.78 eV estimated from the $(\alpha h\nu)^2$ vs $h\nu$ (inset of Figure 3b), and this is in accordance with previous literatures. After the introduction of

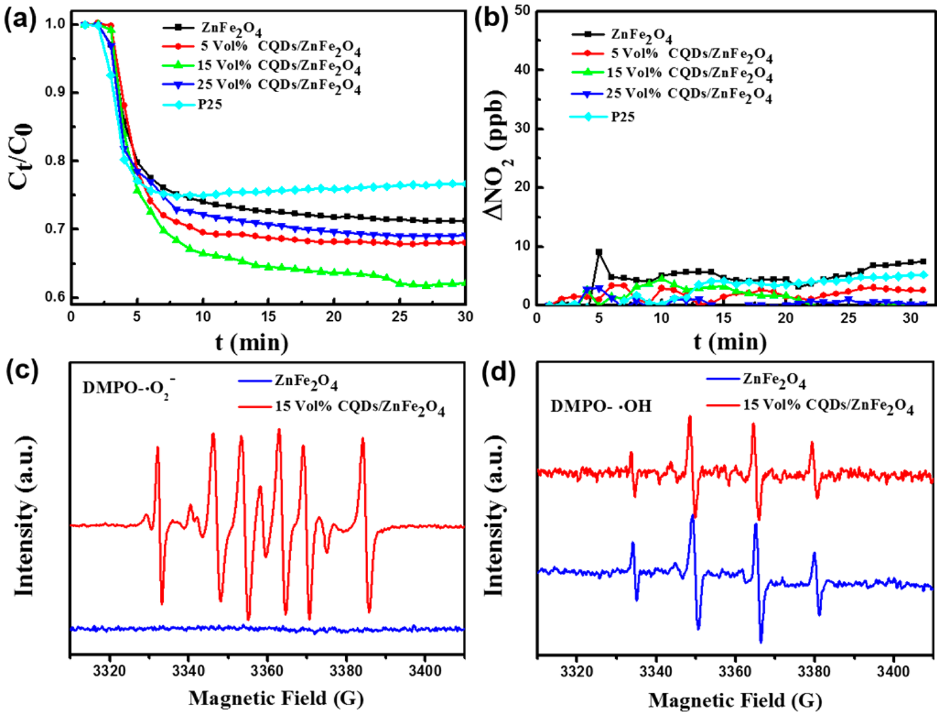

Figure 4. Visible light photocatalytic removal of NO_x (a) and aeration of NO_2 in the gas phase (b) over $ZnFe_2O_4$ and CQDs/$ZnFe_2O_4$ materials; (c) DMPO spin-trapping ESR spectra of $ZnFe_2O_4$ and the 15 Vol% CQDs/$ZnFe_2O_4$ under visible light irradiation in methanol dispersion for DMPO−·O_2^- (c) and in aqueous dispersion for DMPO−·OH (d).

CQDs, the composite shows even stronger absorption in both UV and visible light regions. This result indicates that CQDs enhance the light absorption which may exert a positive effect on generating more electron−hole pairs for photocatalytic reactions. From the inset image in Figure 3b, pure CQDs disperse solution with UV light (365 nm) showed the strong fluorescence, compared with the control sample (water).

In order to probe the separation efficiency of photogenerated charge carriers, photoelectrochemistry analysis was conducted. Figure 3c illustrates the transient photocurrent responses of $ZnFe_2O_4$ and CQDs/$ZnFe_2O_4$ (15 vol %) electrodes in 0.5 M Na_2SO_4 solution under intermittent visible-light irradiation (λ = 420 nm). It can be observed that $ZnFe_2O_4$ exhibits an extremely weak transient photocurrent response upon light exposure, whereas CQDs/$ZnFe_2O_4$ (15 vol %) demonstrates much stronger transient photocurrent response, approximately eight times larger than that of pristine $ZnFe_2O_4$.[17] The result implies that CQDs act as efficient charge transport medium that promotes the separation of electron/hole pairs generated in $ZnFe_2O_4$, and finally contributes to the higher photocurrent response.[62,63] It should be noted the loss of photocurrent (ΔI) exists during the irradiation duration of visible light. This can be rationalized by the consumption of electrons including the trapping of electrons by O_2 and the recombination of electron−hole pairs.[21]

The photocatalytic activity also depends on the position of conduction band (CB) and valence band (VB). Figure 3d shows the valence band XPS spectrum of $ZnFe_2O_4$, from which the valence band maximum (VBM) position can be determined to be 0.76 eV. According to the formula $E_{CBM} = E_{VBM} - E_g$ (CBM: conduction band minimum), and combined with the band gap (E_g) of $ZnFe_2O_4$ (1.78 eV) derived from the UV−vis spectra, the conduction band minimum (E_{CBM}) of $ZnFe_2O_4$ was calculated to be −1.02 eV above E_f. As a result, the photogenerated electrons on the CB of $ZnFe_2O_4$ could reduce O_2 to $\cdot O_2^-$, and the holes on the VB could not oxidize OH^- to produce ·OH since $E°(O_2/\cdot O_2^-)$ was approximate −0.046 eV and $E°(\cdot OH/OH^-)$ was 2.38 eV versus NHE.[64,65]

On the basis of the aforementioned results, the introduction of CQDs resulted in the increase of the surface area and optical absorption, and most importantly, the enhanced separation efficiency of electron−hole pairs which would fundamentally boost the photocatalytc performances.

Photocatalytic Activity, Identification of Reactive Species, and Photocatalytic Mechanism. The photocatalytic oxidation of gas-phase NO_x was conducted under visible light (λ > 420 nm) irradiation at room temperature to evaluate the photocatalytic abilities of $ZnFe_2O_4$ and CQDs/$ZnFe_2O_4$ composites. The NO removal efficiency as a function of time is illustrated in Figure 4a. As observed, $ZnFe_2O_4$ and CQDs/$ZnFe_2O_4$ composites all exhibit superior NO removal performances than commercial P25 photocatalyst, without any significant deactivation in 30 min. Along with the increase of CQDs loading amount, the NO removal efficiency is enhanced, with the best performance achieved on CQDs/$ZnFe_2O_4$ (15 vol %) where 38% of initial nitrogen oxide was removed within 0.5 h. This is significantly higher than those for $ZnFe_2O_4$ (29%) and P25 (23%). When the CQDs loading amount was further increased to 25 vol %, the photocatalytic activity of the composite CQDs/$ZnFe_2O_4$ decreased for NO elimination, however. This may be because the opacity and light scattering of the CQDs reduced the absorption of incident light, which is demonstrated in Figure S1 that CQDs/$ZnFe_2O_4$ (25 vol %) had a similar absorption in both UV and visible light regions with the pure $ZnFe_2O_4$. In addition, the photocatalytic activity tests under UV−vis light irradiation were conducted to evaluate the photocatalytic performance of the as-prepared samples for NO_x elimination from the environment, as shown in Figure

S2a. It is clear to see that all of the CQDs/$ZnFe_2O_4$ samples displayed the higher photocatalytic activity than that of pristine $ZnFe_2O_4$ and commercial P25. Simultaneously, the amount of toxic NO_2 intermediates generated by CQDs/$ZnFe_2O_4$ samples is lower than pristine $ZnFe_2O_4$ and commercial P25 (Figure S2b). Previous reports demonstrated that NO_2 is a byproduct of photocatalytic degradation,[66,67] but NO_2 is more toxic than NO. NO_2 would be released into the air because of desorption when the adsorption site for nitrate is saturated or the concentration of oxidizing species is not satisfied to finish the last reaction. Thus, the selectivity performance of photocatalysts for nitrate formation is very crucial and should be further evaluated. Figure 4b shows that the yield of NO_2 over CQDs/$ZnFe_2O_4$ was lower than that over $ZnFe_2O_4$ and P25. No NO_2 was generated over the CQDs/$ZnFe_2O_4$ (15 vol %) photocatalyst after 30 min. Figure S3 describes NO_2 removal over different photocatalysts. NO_2 removal efficiency is also the highest over CQDs/$ZnFe_2O_4$ (15 vol %). This may rationalize low NO_2 selectivity of CQDs/$ZnFe_2O_4$ (15 vol %) during NO degradation. Moreover, the CQDs/$ZnFe_2O_4$ (15 vol %) photocatalyst can be reused with a similar conversion efficiency as the fresh catalyst for six cycles (see Figure S4). Therefore, we assume that $ZnFe_2O_4$ and CQDs/$ZnFe_2O_4$ are efficient visible-light-driven photocatalysts in terms of NO removal, and the coupling of CQDs further improves the photocatalytic activity and lowers the NO_2 selectivity.

The accumulated amount of NO_2^- and NO_3^- on the surfaces of $ZnFe_2O_4$ and CQDs/$ZnFe_2O_4$ (15 vol %) materials after the photoactivity test was determined using ion chromatography. The amount of NO_3^- accumulated on CQDs/$ZnFe_2O_4$ (15 vol %) surfaces was 4.71 $\mu g/m^2$, which is 1.76 times of that accumulated on the $ZnFe_2O_4$ (2.76 $\mu g/m^2$) (see Table S2), while photocatalytic NO removal on CQDs/$ZnFe_2O_4$(15 vol %) surfaces is 1.31 times of that on $ZnFe_2O_4$. This implies that the introduction of CQDs increased the selectivity of $ZnFe_2O_4$ for nitrate formation. Moreover, an unstable intermediate NO_2^- was detected at low concentration. These results demonstrate that the CQDs/$ZnFe_2O_4$ photocatalyst is promising for air purification under solar light irradiation.

In order to identify the reactive oxygen species involved in photocatalytic removal of NO over $ZnFe_2O_4$ and CQDs/$ZnFe_2O_4$ (15 vol %), ESR spectroscopy was utilized with DMPO as a spin trapping agent, as shown in Figure 4c,d. As observed from Figure 4c, no signal appears for $ZnFe_2O_4$ suggesting that $\cdot O_2^-$ radicals are not produced under visible light, whereas the strong DMPO−$\cdot O_2^-$ related signal with sextet peaks are present over the CQDs/$ZnFe_2O_4$ (15 vol %) sample. This indicates that CQDs played a critical role as the electron reservoir to promote oxygen reduction and generation of super oxidative $\cdot O_2^-$ radicals for NO oxidation. Figure 4d shows that the quartet peaks with relative intensity of 1:2:2:1 are both observed on $ZnFe_2O_4$ and CQDs/$ZnFe_2O_4$ (15 vol %).

The reason the $ZnFe_2O_4$ sample showed no obvious signals of DMPO−$\cdot O_2^-$ was that few electrons were available on the CB to reduce O_2 to generate enough $\cdot O_2^-$, due to the rapid recombination of photoinduced electron−hole pairs. To further unravel the role of the reactive species in NO removal over CQDs/$ZnFe_2O_4$ (15 vol %), the effects of various radical scavengers such as potassium iodide (KI), potassium dichromate ($K_2Cr_2O_7$), and *tert*-butanol (TBA), were examined on NO removal. As demonstrated in Figure S5, all three radical scavengers retarded the photocatalytic degradation of NO. The inhibiting effect of the three scavengers ranks in a sequence of KI ≈ TBA < $K_2Cr_2O_7$, suggesting that electrons play a more important role in NO removal than hydroxyl radicals and holes do. To examine the role of $\cdot O_2^-$ species in NO removal, NO gas was diluted by nitrogen gas instead of air stream. As illustrated in Figure S5, NO elimination was remarkably inhibited. These results further prove that $\cdot O_2^-$ radicals made a significant contribution to NO removal over CQDs/$ZnFe_2O_4$ (15 vol %).

Therefore, the reaction mechanism diagram of the CQDs/$ZnFe_2O_4$ photocatalyst is proposed in Figure 5. Under the irradiation of visible light, the electrons could be excited from the VB to the CB of $ZnFe_2O_4$, leaving holes on the VB. In the absence of CQDs, most of electron−hole pairs quickly recombine and only a small number of electrons can be trapped by O_2 to generate $\cdot O_2^-$ or trapped by Fe^{3+}. As revealed in the ESR spectra that ·OH radicals mainly took part in the photocatalytic reactions, thereby it is assumed that ·OH radicals are transformed from a series of reactions as described below:

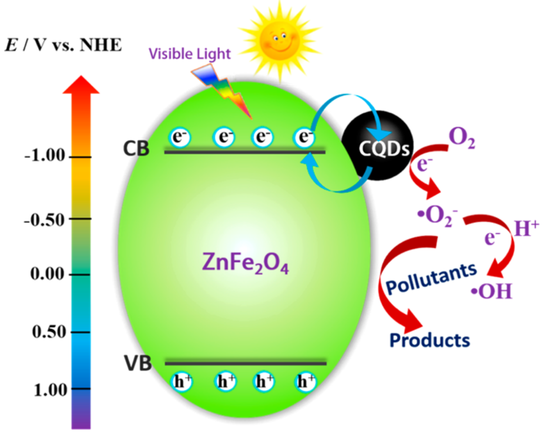

Figure 5. Schematic of the separation and transfer of photo/generated charges in the CQDs/$ZnFe_2O_4$ material combined with the possible reaction mechanism of photocatalysis.

$$ZnFe_2O_4(e^-) + O_2 \rightarrow \cdot O_2^- \quad (1)$$

$$\cdot O_2^- + 2H^+ + e^- \rightarrow H_2O_2 \quad (2)$$

$$H_2O_2 + e^- \rightarrow \cdot OH + OH^- \quad (3)$$

$$Fe^{3+} + e^- \rightarrow Fe^{2+} \quad (4)$$

$$Fe^{2+} + H_2O_2 \rightarrow Fe^{3+} + \cdot OH + OH^- \quad (5)$$

$$Fe^{3+} + OH^- + h\nu \rightarrow Fe^{2+} + \cdot OH \quad (6)$$

In the presence of CQDs, the photogenerated electrons on the CB of $ZnFe_2O_4$ can be transferred to the CQDs, due to their excellent electronic conductivity. The transferred electrons accumulated on the CQDs and were captured by the adsorbed O_2 on the $ZnFe_2O_4$ surface to form superoxide radicals ($\cdot O_2^-$). The excellent adsorptive performance of CQDs could ensure the adsorption of NO, which can then be oxidized to NO_2. Subsequently, NO_2 can be further oxidized to NO_3^- by $\cdot O_2^-$ or ·OH on its surface. It is believed that the $\cdot O_2^-$ radicals play an important role during photocatalysis. Furthermore, hydroxyl radicals were detected and also contributed to NO oxidation in this system. It should be noted that the upconversion PL properties of CQDs can endow $ZnFe_2O_4$ with the efficient utilization of the full spectrum of xenon lamp.[31] And this may further increase the quantum yield of $ZnFe_2O_4$ in visible light system.

Toxicity Assessment and Fluorescence Cellular Imaging. For the potential application in the environment cleanup, the possible cytotoxicity of $ZnFe_2O_4$ and CQDs/$ZnFe_2O_4$ was examined through the MTT assay with A549 cells as a model. Cells were exposed to concentrations of 0.5, 5, 10, 25, 50, and 100 μg mL^{-1} of dispersed sample solutions. As shown in Figure 6a, the cell viabilities exhibited the concentration-dependent manner for both nanoparticles, and $ZnFe_2O_4$ was more lethal to A549 cells than CQDs/$ZnFe_2O_4$. $ZnFe_2O_4$ stimulated proliferation at a very low concentration of 0.5 μg mL^{-1}, and cell viability decreased with the enhancement of NP concentration. However, the cell viability of A549 cells treated by different concentration of CQDs/$ZnFe_2O_4$ always keeps the relatively high value (over 80%), even at the concentration of 100 μg mL^{-1}, revealing the good biocompatibility and low cytotoxicity of CQDs/$ZnFe_2O_4$ for A549 cells.

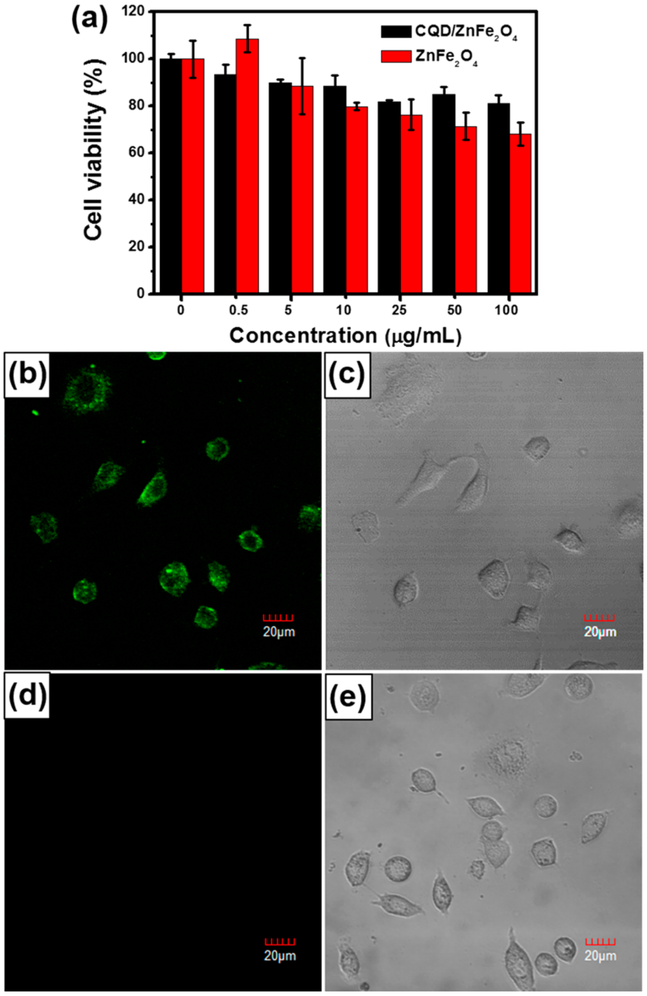

Figure 6. (a) Relative viability of A549 cells after incubation of 24 h with different concentration of $ZnFe_2O_4$ and 15 vol % CQDs/$ZnFe_2O_4$. (b−e) Intracellular delivery of $ZnFe_2O_4$ and 15 vol % CQDs/$ZnFe_2O_4$ under bright-field and at an excitation wavelength of 488 nm.

In vitro bioimaging study was carried out using A549 cells incubated with $ZnFe_2O_4$ and CQDs/$ZnFe_2O_4$. Figure 6b,c shows the bright-field and one-photon confocal fluorescent images of the A549 cells which were incubated with 50 μg mL^{-1} of CQDs/$ZnFe_2O_4$ in the medium for 1 h, and then well washed. The bright-field image of the cells is clear visualized and cells exhibit brightly green color upon illumination at 488 nm. The majority of the fluorescent signals of CQDs/$ZnFe_2O_4$ appeared to come from the cell membrane and cytoplasmic area of A549 cells. In addition, extremely weak luminescence can be observed in the cell nucleus, demonstrating that few CQDs/$ZnFe_2O_4$NPs enter into the inner nuclei, thus causing lower toxicity. In contrast, no fluorescence can be observed in the cells incubated with $ZnFe_2O_4$ (Figure 6d) under the same conditions. The bright-field image shows that the cells became less adherent and exhibited severer toxicity (Figure 6e). These results were coincident with that of previous MTT assay.

In summary, CQDs/$ZnFe_2O_4$ displayed enhanced photocatalytic activities and selectivity for nitrate formation as compared with pristine $ZnFe_2O_4$ under visible light ($\lambda > 420$ nm) irradiation. The CQDs are believed to act as an electron reservoir and transporter as well as a powerful energy-transfer component during the photocatalysis of CQDs/$ZnFe_2O_4$. The toxicity assessment authenticated good biocompatibility and low cytotoxicity of CQDs/$ZnFe_2O_4$. The results of this study indicate CQDs/$ZnFe_2O_4$ is a promising photocatalyst for air purification.

■ ASSOCIATED CONTENT

Ⓢ Supporting Information

The Supporting Information is available free of charge on the ACS Publications website at DOI: 10.1021/acs.est.6b04460.

> Additional detail information including BET specific surface area (S_{BET}), pore volume and average pore diameter results, UV−visible diffuse reflectance spectra of $ZnFe_2O_4$ and CQDs/$ZnFe_2O_4$, UV−vis light photocatalytic removal of NO_x over $ZnFe_2O_4$ and CQDs/$ZnFe_2O_4$, visible light photocatalytic removal efficiency for NO_2, and cycle runs experiments and effects of different scavengers on NO_x removal (PDF)

■ AUTHOR INFORMATION

Corresponding Author

*Tel: 86-29-6233 6261; e-mail: huangyu@ieecas.cn (Y.H.).

ORCID

Yu Huang: 0000-0003-3334-4849

Notes

The authors declare no competing financial interest.

■ ACKNOWLEDGMENTS

This research was financially supported by the National Key Research and Development Program of China (2016YFA0203000), the National Science Foundation of China (41401567, 41573138) and the “Strategic Priority Research Program” of the Chinese Academy of Sciences (Grant No. XDB05000000). Y.H. is also supported by the “Hundred Talent Program” of the Chinese Academy of Sciences.

■ REFERENCES

(1) Gomez Alvarez, E.; Wortham, H.; Strekowski, R.; Zetzsch, C.; Gligorovski, S. Atmospheric Photosensitized Heterogeneous and Multiphase Reactions: From Outdoors to Indoors. *Environ. Sci. Technol.* **2012**, *46* (4), 1955−1963.

(2) Huang, R.-J.; Zhang, Y.; Bozzetti, C.; Ho, K.-F.; Cao, J.-J.; Han, Y.; Daellenbach, K. R.; Slowik, J. G.; Platt, S. M.; Canonaco, F.; Zotter, P.; Wolf, R.; Pieber, S. M.; Bruns, E. A.; Crippa, M.; Ciarelli, G.; Piazzalunga, A.; Schwikowski, M.; Abbaszade, G.; Schnelle-Kreis, J.; Zimmermann, R.; An, Z.; Szidat, S.; Baltensperger, U.; El Haddad, I.; Prevot, A. S. H. High secondary aerosol contribution to particulate pollution during haze events in China. *Nature* **2014**, *514* (7521), 218−222.

(3) Zhao, B.; Wang, S. X.; Liu, H.; Xu, J. Y.; Fu, K.; Klimont, Z.; Hao, J. M.; He, K. B.; Cofala, J.; Amann, M. NOx emissions in China: historical trends and future perspectives. *Atmos. Chem. Phys.* **2013**, *13* (19), 9869−9897.

(4) Tanaka, T.; Teramura, K.; Arakaki, K.; Funabiki, T. Photoassisted NO reduction with NH_3 over TiO_2 photocatalyst. *Chem. Commun.* **2002**, *22*, 2742−2743.

(5) Macleod, N.; Cropley, R.; Keel, J. M.; Lambert, R. M. Exploiting the synergy of titania and alumina in lean NO(x) reduction: in situ ammonia generation during the Pd/TiO(2)/Al(2)O(3)-catalysed H(2)/CO/NO/O(2) reaction. *J. Catal.* **2004**, *221* (1), 20−31.

(6) Granger, P.; Parvulescu, V. I. Catalytic NOx Abatement Systems for Mobile Sources: From Three-Way to Lean Burn after-Treatment Technologies. *Chem. Rev.* **2011**, *111* (5), 3155−3207.

(7) Ma, J.; He, H.; Liu, F. Effect of Fe on the photocatalytic removal of NOx over visible light responsive Fe/TiO_2 catalysts. *Appl. Catal., B* **2015**, *179*, 21−28.

(8) Ângelo, J.; Andrade, L.; Madeira, L. M.; Mendes, A. An overview of photocatalysis phenomena applied to NOx abatement. *J. Environ. Manage.* **2013**, *129*, 522−539.

(9) Lasek, J.; Yu, Y.-H.; Wu, J. C. S. Removal of NOx by photocatalytic processes. *J. Photochem. Photobiol., C* **2013**, *14*, 29−52.

(10) Balbuena, J.; Cruz-Yusta, M.; Cuevas, A. L.; López-Escalante, M. C.; Martín, F.; Pastor, A.; Sánchez, L. Enhanced activity of α-Fe_2O_3 for photocatalytic NO removal. *RSC Adv.* **2016**, *6* (95), 92917−92922.

(11) Balbuena, J.; Carraro, G.; Cruz, M.; Gasparotto, A.; Maccato, C.; Pastor, A.; Sada, C.; Barreca, D.; Sanchez, L. Advances in photocatalytic NOx abatement through the use of Fe_2O_3/TiO_2 nanocomposites. *RSC Adv.* **2016**, *6* (78), 74878−74885.

(12) Fan, Y.; Lu, X.; Ni, Y.; Zhang, H.; Zhao, L.; Chen, J.; Sun, C. Destruction of Polychlorinated Aromatic Compounds by Spinel-Type Complex Oxides. *Environ. Sci. Technol.* **2010**, *44* (8), 3079−3084.

(13) Fan, Y.; Lu, X.; Ni, Y.; Zhang, H.; Zhu, M.; Li, Y.; Chen, J. Catalytic destruction of chlorinated aromatic pollutants over mesoporous Cu_xMg_1-xAl_2O_4 spinel oxides. *Appl. Catal., B* **2011**, *101* (3−4), 606−612.

(14) Zhang, T.; Zhu, H.; Croue, J.-P. Production of Sulfate Radical from Peroxymonosulfate Induced by a Magnetically Separable $CuFe_2O_4$ Spinel in Water: Efficiency, Stability, and Mechanism. *Environ. Sci. Technol.* **2013**, *47* (6), 2784−2791.

(15) Tezuka, K.; Kogure, M.; Shan, Y. J. Photocatalytic degradation of acetic acid on spinel ferrites MFe_2O_4 (M = Mg, Zn, and Cd). *Catal. Commun.* **2014**, *48*, 11−14.

(16) Paul, B.; Bhuyan, B.; Purkayastha, D. D.; Dhar, S. S.; Behera, S. Facile synthesis of spinel $CuCr_2O_4$ nanoparticles and studies of their photocatalytic activity in degradation of some selected organic dyes. *J. Alloys Compd.* **2015**, *648*, 629−635.

(17) Dom, R.; Chary, A. S.; Subasri, R.; Hebalkar, N. Y.; Borse, P. H. Solar hydrogen generation from spinel $ZnFe_2O_4$ photocatalyst: effect of synthesis methods. *Int. J. Energy Res.* **2015**, *39* (10), 1378−1390.

(18) Song, H.; Zhu, L.; Li, Y.; Lou, Z.; Xiao, M.; Ye, Z. Preparation of $ZnFe_2O_4$ nanostructures and highly efficient visible-light-driven hydrogen generation with the assistance of nanoheterostructures. *J. Mater. Chem. A* **2015**, *3* (16), 8353−8360.

(19) Li, X.; Hou, Y.; Zhao, Q.; Teng, W.; Hu, X.; Chen, G. Capability of novel $ZnFe_2O_4$ nanotube arrays for visible-light induced degradation of 4-chlorophenol. *Chemosphere* **2011**, *82* (4), 581−586.

(20) Zhang, W.; Wang, M.; Zhao, W.; Wang, B. Magnetic composite photocatalyst $ZnFe_2O_4$/$BiVO_4$: synthesis, characterization, and visible-light photocatalytic activity. *Dalton. Trans.* **2013**, *42* (43), 15464−15474.

(21) Yang, D.; Feng, J.; Jiang, L.; Wu, X.; Sheng, L.; Jiang, Y.; Wei, T.; Fan, Z. Photocatalyst Interface Engineering: Spatially Confined Growth of $ZnFe_2O_4$ within Graphene Networks as Excellent Visible-Light-Driven Photocatalysts. *Adv. Funct. Mater.* **2015**, *25* (45), 7080−7087.

(22) Lv, H.; Ma, L.; Zeng, P.; Ke, D.; Peng, T. Synthesis of floriated $ZnFe_2O_4$ with porous nanorod structures and its photocatalytic hydrogen production under visible light. *J. Mater. Chem.* **2010**, *20* (18), 3665−3672.

(23) Yao, Y.; Qin, J.; Chen, H.; Wei, F.; Liu, X.; Wang, J.; Wang, S. One-pot approach for synthesis of N-doped TiO_2/$ZnFe_2O_4$ hybrid as an efficient photocatalyst for degradation of aqueous organic pollutants. *J. Hazard. Mater.* **2015**, *291*, 28−37.

(24) Guo, X.; Zhu, H.; Li, Q. Visible-light-driven photocatalytic properties of ZnO/$ZnFe_2O_4$ core/shell nanocable arrays. *Appl. Catal., B* **2014**, *160−161*, 408−414.

(25) Fu, Y.; Wang, X. Magnetically Separable $ZnFe_2O_4$-Graphene Catalyst and its High Photocatalytic Performance under Visible Light Irradiation. *Ind. Eng. Chem. Res.* **2011**, *50* (12), 7210−7218.

(26) Khadgi, N.; Li, Y.; Upreti, A. R.; Zhang, C.; Zhang, W.; Wang, Y.; Wang, D. Enhanced Photocatalytic Degradation of 17-Ethinylestradiol Exhibited by Multifunctional $ZnFe_2O_4$-Ag/rGO Nanocomposite Under Visible Light. *Photochem. Photobiol.* **2016**, *92* (2), 238−246.

(27) Qu, Q.; Zhu, A.; Shao, X.; Shi, G.; Tian, Y. Development of a carbon quantum dots-based fluorescent Cu^{2+} probe suitable for living cell imaging. *Chem. Commun.* **2012**, *48* (44), 5473−5475.

(28) Mirtchev, P.; Henderson, E. J.; Soheilnia, N.; Yip, C. M.; Ozin, G. A. Solution phase synthesis of carbon quantum dots as sensitizers for nanocrystalline TiO_2 solar cells. *J. Mater. Chem.* **2012**, *22* (4), 1265−1269.

(29) Zhu, S.; Zhang, J.; Qiao, C.; Tang, S.; Li, Y.; Yuan, W.; Li, B.; Tian, L.; Liu, F.; Hu, R.; Gao, H.; Wei, H.; Zhang, H.; Sun, H.; Yang, B. Strongly green-photoluminescent graphene quantum dots for bioimaging applications. *Chem. Commun.* **2011**, *47* (24), 6858−6860.

(30) Li, H.; Kang, Z.; Liu, Y.; Lee, S.-T. Carbon nanodots: synthesis, properties and applications. *J. Mater. Chem.* **2012**, *22* (46), 24230−24253.

(31) Di, J.; Xia, J.; Ge, Y.; Li, H.; Ji, H.; Xu, H.; Zhang, Q.; Li, H.; Li, M. Novel visible-light-driven CQDSs/Bi_2WO_6 hybrid materials with enhanced photocatalytic activity toward organic pollutants degradation and mechanism insight. *Appl. Catal., B* **2015**, *168−169*, 51−61.

(32) Cao, L.; Wang, X.; Meziani, M. J.; Lu, F. S.; Wang, H. F.; Luo, P. J. G.; Lin, Y.; Harruff, B. A.; Veca, L. M.; Murray, D.; Xie, S. Y.; Sun, Y. P. Carbon dots for multiphoton bioimaging. *J. Am. Chem. Soc.* **2007**, *129* (37), 11318−11319.

(33) Li, H.; He, X.; Kang, Z.; Huang, H.; Liu, Y.; Liu, J.; Lian, S.; Tsang, C. H. A.; Yang, X.; Lee, S.-T. Water-Soluble Fluorescent Carbon Quantum Dots and Photocatalyst Design. *Angew. Chem., Int. Ed.* **2010**, *49* (26), 4430−4434.

(34) Shen, J. H.; Zhu, Y. H.; Chen, C.; Yang, X. L.; Li, C. Z. Facile preparation and upconversion luminescence of graphene quantum dots. *Chem. Commun.* **2011**, *47* (9), 2580−2582.

(35) Zhang, X.; Wang, F.; Huang, H.; Li, H.; Han, X.; Liu, Y.; Kang, Z. Carbon quantum dot sensitized TiO_2 nanotube arrays for photoelectrochemical hydrogen generation under visible light. *Nanoscale* **2013**, *5* (6), 2274.

(36) Wang, J.; Gao, M. M.; Ho, G. W. Bidentate-complex-derived TiO_2/carbon dot photocatalysts: in situ synthesis, versatile heterostructures, and enhanced H_2 evolution. *J. Mater. Chem. A* **2014**, *2* (16), 5703−5709.

(37) Yu, H.; Zhao, Y.; Zhou, C.; Shang, L.; Peng, Y.; Cao, Y.; Wu, L.-Z.; Tung, C.-H.; Zhang, T. Carbon quantum dots/TiO_2 composites for efficient photocatalytic hydrogen evolution. *J. Mater. Chem. A* **2014**, *2* (10), 3344−3351.

(38) Zhang, H. C.; Ming, H.; Lian, S. Y.; Huang, H.; Li, H. T.; Zhang, L. L.; Liu, Y.; Kang, Z. H.; Lee, S. T. Fe_2O_3/carbon quantum dots complex photocatalysts and their enhanced photocatalytic activity under visible light. *Dalton Trans.* **2011**, *40* (41), 10822−10825.

(39) Yu, B. Y.; Kwak, S.-Y. Carbon quantum dots embedded with mesoporous hematite nanospheres as efficient visible light-active photocatalysts. *J. Mater. Chem.* **2012**, *22* (17), 8345−8353.

(40) Zhang, H.; Huang, H.; Ming, H.; Li, H.; Zhang, L.; Liu, Y.; Kang, Z. Carbon quantum dots/Ag_3PO_4 complex photocatalysts with enhanced photocatalytic activity and stability under visible light. *J. Mater. Chem.* **2012**, *22* (21), 10501−10506.

(41) Li, H.; Zhang, X.; MacFarlane, D. R. Carbon Quantum Dots/Cu_2O Heterostructures for Solar-Light-Driven Conversion of CO_2 to Methanol. *Adv. Energy Mater.* **2015**, *5* (5), 1−6.

(42) Li, H.; Liu, R.; Liu, Y.; Huang, H.; Yu, H.; Ming, H.; Lian, S.; Lee, S.-T.; Kang, Z. Carbon quantum dots/Cu_2O composites with protruding nanostructures and their highly efficient (near) infrared photocatalytic behavior. *J. Mater. Chem.* **2012**, *22* (34), 17470−17475.

(43) Yu, H.; Zhang, H.; Huang, H.; Liu, Y.; Li, H.; Ming, H.; Kang, Z. ZnO/carbon quantum dots nanocomposites: one-step fabrication and superior photocatalytic ability for toxic gas degradation under visible light at room temperature. *New J. Chem.* **2012**, *36* (4), 1031−1035.

(44) Liu, Y.; Yu, Y.-X.; Zhang, W.-D. Carbon quantum dots-doped CdS microspheres with enhanced photocatalytic performance. *J. Alloys Compd.* **2013**, *569*, 102−110.

(45) Liu, J.; Liu, Y.; Liu, N.; Han, Y.; Zhang, X.; Huang, H.; Lifshitz, Y.; Lee, S.-T.; Zhong, J.; Kang, Z. Metal-free efficient photocatalyst for stable visible water splitting via a two-electron pathway. *Science* **2015**, *347*, 970−974.

(46) Tang, D.; Zhang, H.; Huang, H.; Liu, R.; Han, Y.; Liu, Y.; Tong, C.; Kang, Z. Carbon quantum dots enhance the photocatalytic performance of $BiVO_4$ with different exposed facets. *Dalton. Trans.* **2013**, *42* (18), 6285−6289.

(47) Di, J.; Xia, J.; Ji, M.; Li, H.; Xu, H.; Li, H.; Chen, R. The synergistic role of carbon quantum dots for the improved photocatalytic performance of Bi_2MoO_6. *Nanoscale* **2015**, *7* (26), 11433−11443.

(48) Di, J.; Xia, J. X.; Ji, M. X.; Wang, B.; Yin, S.; Zhang, Q.; Chen, Z. G.; Li, H. M. Carbon Quantum Dots Modified BiOCl Ultrathin Nanosheets with Enhanced Molecular Oxygen Activation Ability for Broad Spectrum Photocatalytic Properties and Mechanism Insight. *ACS Appl. Mater. Interfaces* **2015**, *7* (36), 20111−2023.

(49) Di, J.; Xia, J.; Ji, M.; Wang, B.; Yin, S.; Xu, H.; Chen, Z.; Li, H. Carbon Quantum Dots Induced Ultrasmall BiOI Nanosheets with Assembled Hollow Structures for Broad Spectrum Photocatalytic Activity and Mechanism Insight. *Langmuir* **2016**, *32* (8), 2075−2084.

(50) Hu, H.; Li, Q.; Jiang, L.; Zou, Y.; Duan, J.; Sun, Z. Genome-wide transcriptional analysis of silica nanoparticle-induced toxicity in zebrafish embryos. *Toxicol. Res.* **2016**, *5* (2), 609−620.

(51) Wang, Z.; Xu, L.; Zhao, J.; Wang, X.; White, J. C.; Xing, B. CuO Nanoparticle Interaction with Arabidopsis thaliana: Toxicity, Parent-Progeny Transfer, and Gene Expression. *Environ. Sci. Technol.* **2016**, *50* (11), 6008−16.

(52) Kim, I.-S.; Baek, M.; Choi, S.-J. Comparative Cytotoxicity of Al_2O_3, CeO_2, TiO_2 and ZnO Nanoparticles to Human Lung Cells. *J. Nanosci. Nanotechnol.* **2010**, *10* (5), 3453−3458.

(53) Bastos, V.; Ferreira de Oliveira, J. M. P.; Brown, D.; Jonhston, H.; Malheiro, E.; Daniel-da-Silva, A. L.; Duarte, I. F.; Santos, C.; Oliveira, H. The influence of Citrate or PEG coating on silver nanoparticle toxicity to a human keratinocyte cell line. *Toxicol. Lett.* **2016**, *249*, 29−41.

(54) Wu, H.; Mi, C.; Huang, H.; Han, B.; Li, J.; Xu, S. Solvothermal synthesis of green-fluorescent carbon nanoparticles and their application. *J. Lumin.* **2012**, *132* (6), 1603−1607.

(55) Havrdova, M.; Hola, K.; Skopalik, J.; Tomankova, K.; Petr, M.; Cepe, K.; Polakova, K.; Tucek, J.; Bourlinos, A. B.; Zboril, R. Toxicity of carbon dots - Effect of surface functionalization on the cell viability, reactive oxygen species generation and cell cycle. *Carbon* **2016**, *99*, 238−248.

(56) Zou, Y. J.; Jin, C. Y.; Su, Y.; Li, J.; Zhu, B. S. Water soluble and insoluble components of urban $PM_{2.5}$ and their cytotoxic effects on epithelial cells (A549) *in vitro*. *Environ. Pollut.* **2016**, *212*, 627−635.

(57) Thankachan, R. M.; Rahman, M. M.; Sultana, I.; Glushenkov, A. M.; Thomas, S.; Kalarikkal, N.; Chen, Y. Enhanced lithium storage in $ZnFe_2O_4$−C nanocomposite produced by a low-energy ball milling. *J. Power Sources* **2015**, *282*, 462−470.

(58) Hou, Y.; Li, X.-Y.; Zhao, Q.-D.; Quan, X.; Chen, G.-H. Electrochemical Method for Synthesis of a $ZnFe_2O_4$/TiO_2 Composite Nanotube Array Modified Electrode with Enhanced Photoelectrochemical Activity. *Adv. Funct. Mater.* **2010**, *20* (13), 2165−2174.

(59) Cai, C.; Zhang, Z.; Liu, J.; Shan, N.; Zhang, H.; Dionysiou, D. D. Visible light-assisted heterogeneous Fenton with $ZnFe_2O_4$ for the degradation of Orange II in water. *Appl. Catal., B* **2016**, *182*, 456−468.

(60) Ibrahim, I.; Ali, I. O.; Salama, T. M.; Bahgat, A. A.; Mohamed, M. M. Synthesis of magnetically recyclable spinel ferrite (MFe_2O_4, M = Zn, Co, Mn) nanocrystals engineered by sol gel-hydrothermal technology: High catalytic performances for nitroarenes reduction. *Appl. Catal., B* **2016**, *181*, 389−402.

(61) Huang, Y.-F.; Zhou, X.; Zhou, R.; Zhang, H.; Kang, K.-B.; Zhao, M.; Peng, Y.; Wang, Q.; Zhang, H.-L.; Qiu, W.-Y. One-Pot Synthesis of Highly Luminescent Carbon Quantum Dots and Their Nontoxic Ingestion by Zebrafish for In Vivo Imaging. *Chem. - Eur. J.* **2014**, *20* (19), 5640−5648.

(62) Yen, C.-W.; Chu, L.-K.; El-Sayed, M. A. Plasmonic Field Enhancement of the Bacteriorhodopsin Photocurrent during Its Proton Pump Photocycle. *J. Am. Chem. Soc.* **2010**, *132* (21), 7250−7251.

(63) Zhang, J.; Zhang, M.; Yang, C.; Wang, X. Nanospherical Carbon Nitride Frameworks with Sharp Edges Accelerating Charge Collection and Separation at a Soft Photocatalytic Interface. *Adv. Mater.* **2014**, *26* (24), 4121−4126.

(64) Di, J.; Xia, J.; Ji, M.; Xu, L.; Yin, S.; Zhang, Q.; Chen, Z.; Li, H. Carbon quantum dots in situ coupling to bismuth oxyiodide via reactable ionic liquid with enhanced photocatalytic molecular oxygen activation performance. *Carbon* **2016**, *98*, 613−623.

(65) Xia, J.; Di, J.; Li, H.; Xu, H.; Li, H.; Guo, S. Ionic liquid-induced strategy for carbon quantum dots/BiOX (X = Br, Cl) hybrid nanosheets with superior visible light-driven photocatalysis. *Appl. Catal., B* **2016**, *181*, 260−269.

(66) Zhang, Q.; Huang, Y.; Xu, L.; Cao, J.-j.; Ho, W.; Lee, S. C. Visible-Light-Active Plasmonic Ag-$SrTiO_3$ Nanocomposites for the Degradation of NO in Air with High Selectivity. *ACS Appl. Mater. Interfaces* **2016**, *8* (6), 4165−4174.

(67) Fujiwara, K.; Mueller, U.; Pratsinis, S. E. Pd Subnano-Clusters on TiO_2 for Solar-Light Removal of NO. *ACS Catal.* **2016**, *6* (3), 1887−1893.